

Sensor and Simulation Notes

Note 347

25 October 1992

ANALYSIS OF BLOCKAGE EFFECTS ON  
TEM-FED PARABOLOIDAL REFLECTOR ANTENNAS

Prof. Y.Rahmat-Samii

Department of Electrical Engineering, UCLA, Los Angeles, CA  
(Consultant to: Pro-Tech, 3708 Mt. Diablo Blvd., #215, Lafayette, CA )

CLEARED  
FOR PUBLIC RELEASE  
PL/PA 10 NOV 92

Abstract

TEM-fed paraboloidal reflector antennas are being considered as a viable solution for generating wideband signals. An issue of design consideration is to identify the effects of the blockage on the performance of these type of reflector antennas. In this note, the blockage effects of the two-arm and four-arm TEM-fed structures are investigated. Both gain performance degradation and sidelobe degradation are studied. The study has been performed for range of frequencies for which the antenna dimensions are more than three wavelengths. Furthermore, it is assumed that the physical optics diffraction analysis with the current-shadowing approach provides proper estimates for these type of evaluation. Initially, we have considered 1 and 10 dB tapers in the illuminating field. Future reports will consider actual TEM field illumination of the paraboloidal reflector.

PL 92-0779

## CONTENTS

<u>Section</u>	<u>Page</u>
1. INTRODUCTION	3
2. JACOBI-BESSEL SERIES EXPANSION	13
3. REFLECTOR ANTENNA ANALYSIS	22
References	33

## ACKNOWLEDGEMENT

This report was written by Prof. Yahya Rahmat-Samii of the Department of Electrical Engineering, University of California, Los Angeles Campus, in his capacity as a consultant to Pro-Tech in Lafayette, CA. The author and Dr. D.V. Giri of Pro-Tech are thankful to Capt. L. Miner, Phillips Laboratory, Kirtland AFB, New Mexico for valuable discussions and support.

## 1. INTRODUCTION

Among different reflector antenna configurations that have been studied in the past [1 to 8] , TEM-fed reflector antennas have received much attention recently [9 to 13] for wideband applications. Figure 1.1 demonstrates possible design configurations. It is observed that the plates allow for the generation of spherical TEM waves which are then scattered from the paraboloidal reflector surface. In this investigation, our attention is primarily focussed on the configuration as shown in figure 1.1. There are other options which could utilize edge-on guiding structures for the spherical TEM waves. Such an option is not considered in the present study.

From the design configuration of figure 1.1, it is clear that the scattered field from the reflector is blocked by the wave-guiding structure. It is the purpose of this note to analyze and evaluate the effects of these blockages on the overall performance of the reflector. We limit our study to the frequency ranges for which the physical optics modeling of the reflector is accurate. This range will typically allow one to consider reflectors with diameters no less than three wavelengths. Next, it is assumed that the blockage effect can be interpreted as the geometrical shadowing effects in terms of the equivalent aperture distribution. Numerical results will be presented for the boresight gain loss and sidelobe degradation for different parameters of the guiding structure. The parameters for numerical purposes are: reflector diameter  $D = 5\text{m}$  , focal length  $f = 2\text{m}$ ,  $(f/D) = 0.4$ , characteristic impedance of the TEM horn is nominally 400 Ohms. The formulation is for a general  $N$  number of feed arms and in the numerical study, we have considered 2 and 4 arms, at frequencies of 3GHz, 1GHz, 0.5GHz and 0.2GHz. The illuminating field is considered to have a tapered distribution of 1 and 10 dB. These numbers are for numerical illustrative purposes only. An actual TEM distribution can be used as the illuminating field if desired in future studies.

### A. Brief description of the Formulation

It is well known that the physical optics diffraction analysis of reflector antennas provide accurate results for antenna geometries that are larger than three wavelengths. This is in particular true for performance ranges including several first sidelobes. In order to construct the physical optics current on the curved surface of the antenna, it is assumed that the incident field of the feed is known. Since the main interest of this work is to examine the effects of blockage due to the feeding structure of the TEM-feed configuration, we model the illumination

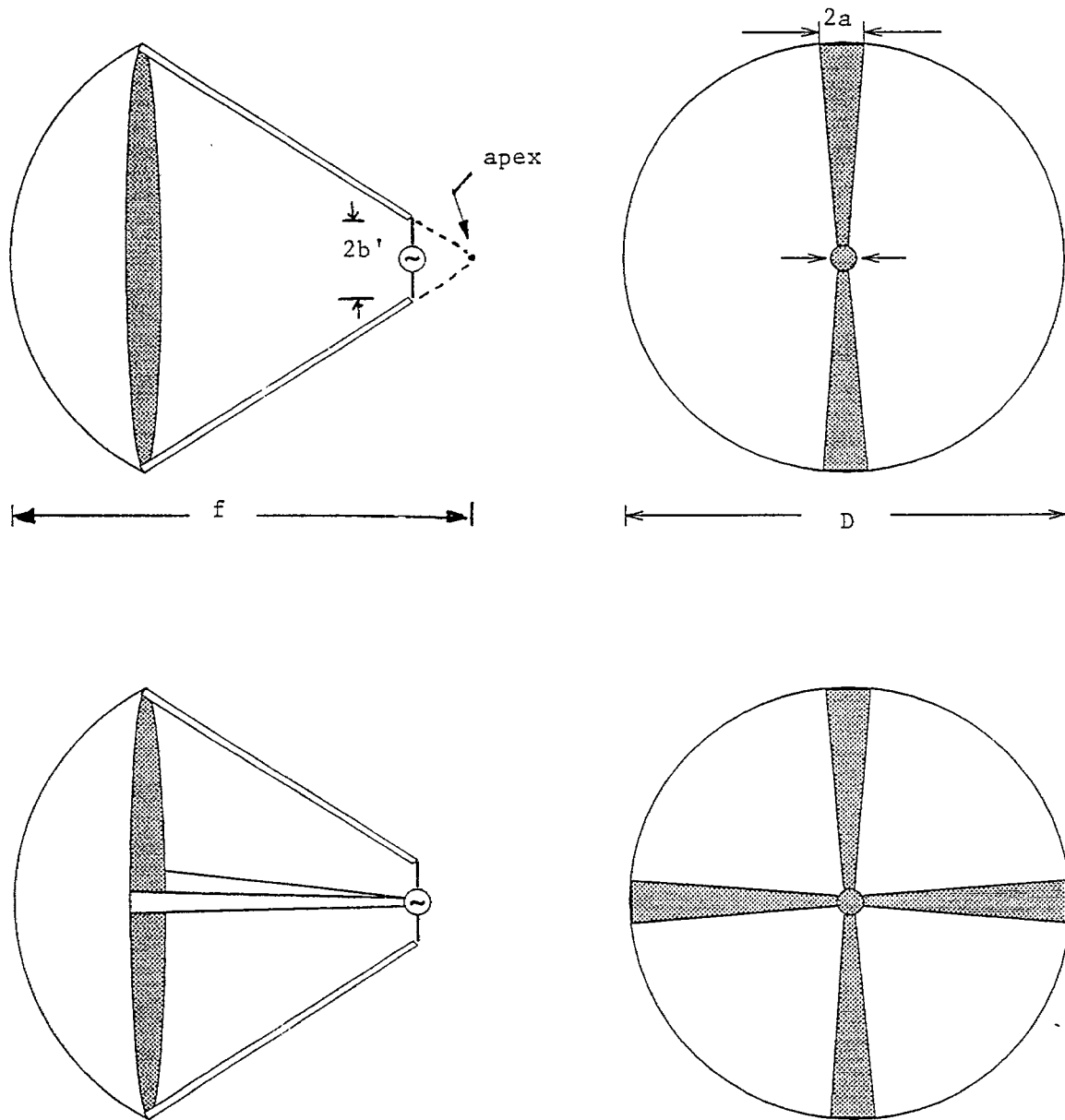


Figure 1.1 Antenna Configurations for two-arm and four-arm TEM-fed reflectors  
(e.g.,  $D = 5\text{m}$ ,  $f = 2\text{m}$ ,  $2a = 0.72\text{m}$ ,  $2b = D = 5\text{m}$ ,  $2b' = 0.1\text{m}$ )

by  $\cos^2\theta$  type feed patterns with spherical wavefront centered at the location of the feed. Different feed tapers are addressed to demonstrate the effects of illumination tapers on the reflector performance. If need be, actual spherical TEM field illumination may also be used in future studied.

In this study, we have utilized the Physical Optics diffraction analysis of the reflector antennas based on the application of the Jacobi-Bessel expansion technique. The usefulness of this technique has been presented by this author in previous publications. Additionally, the important steps of this technique are documented in sections 2 and 3 of this note. The numerical analysis is capable of including blockage effects as shown in figure 1.2. As can be seen from this figure, we can include N number of feed arms in this study. For numerical purposes we have considered  $N = 0, 2$  and  $4$ . The process of implementation of this blockage is based on the assumption that the exit wavefront from the parabolic surface is planar, and therefore, the blockage primarily manifests itself as shadowing the exit wavefront. This concept is implemented by essentially forcing the current to be zero in the areas of the reflector for which the projection matches the projection of the blocking structure in the exit aperture.

## B. Representative Results

For the antenna configuration shown in figure 1.1, numerical analyses have been performed at different frequencies and for two different illumination tapers. The parameters are summarized below:

the reflector diameter	D	=	5 m
focal length	f	=	2 m
focal length/dia.	f/D	=	0.4
TEM impedance	$Z_c$	=	400 Ohms (nominal)
full plate width	2a	=	0.72 m
full plate separation	2b	=	5 m
width /separation	b/a	=	6.99

As mentioned earlier, we have used  $\cos^2\theta$  feed model to define the illumination from the feed. Both low and high tapers have been investigated. It is recognized that these tapers are not necessarily the same as that of TEM mode. In particular,

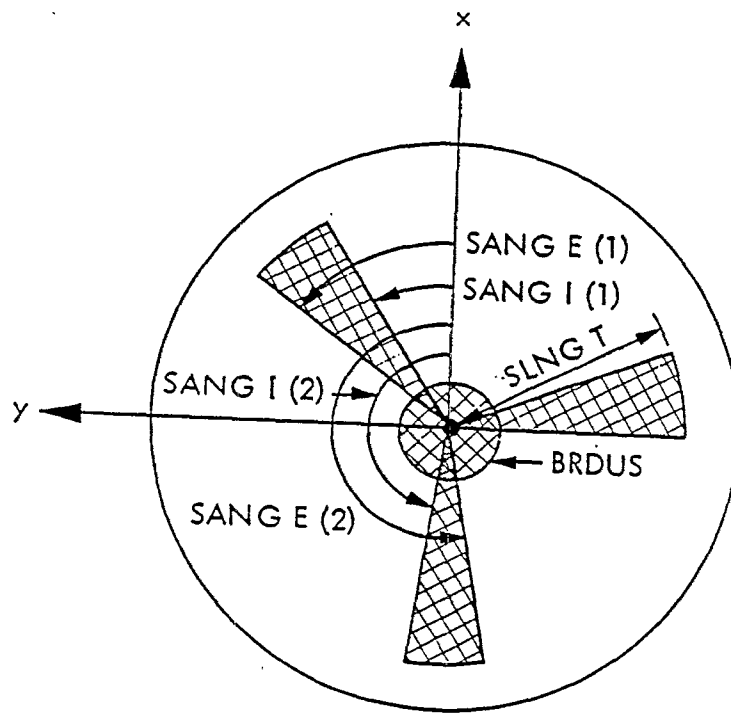


Figure 1.2      Geometry of the central blockage and feed arms  
 based on geometrical shadowing

the low taper  $\cos^2 q$  model does result in an excessive spillover energy. Therefore, the directivity may not be representative, but the gain loss will be. Table 1.1 summarizes the gain loss values at four different frequencies, two different illumination tapers and three different blockage arrangements. As expected the gain loss values are predominantly controlled by the area of the shadowed regions. For all of the above cases, the radiated far field patterns are shown in subsequent figures 1.3 to 1.6. These figures demonstrate how the blockage affects the sidelobe formations. The blockage has a more distinct effect on the sidelobes rather than on the main lobe. Based on these results, it is observed that the geometry of figure 1.1 does not severely distort the radiated patterns at frequencies for which the reflector diameter is at least 3 wavelengths long. For a reflector dia. of 5m, this frequency is roughly 200 MHz. For lower frequencies, where the reflector diameter is less than 3 wavelengths long, additional studies based on the application of the method of moments or physical optics hybrid method (POHM) will become necessary.

TABLE 1.1 Gainloss versus Blockage

Freq (GHz)	Taper (dB)	# struts (feed arms)	Directivity (dB)	Gainloss (dB)
3	10	0	43.097	-
		2	42.138	0.959
		4	41.659	1.438
	1	0	39.061	-
		2	38.105	0.956
		4	37.625	1.436
1	10	0	33.555	-
		2	32.596	0.959
		4	32.116	1.439
	1	0	29.519	-
		2	28.563	0.956
		4	28.083	1.436
0.5	10	0	27.534	-
		2	26.575	0.959
		4	26.096	1.438
	1	0	23.498	-
		2	22.542	0.956
		4	22.062	1.436
0.2	10	0	19.576	-
		2	18.616	0.960
		4	18.137	1.439
	1	0	15.539	-
		2	14.583	0.956
		4	14.104	1.435

f = 3 GHz

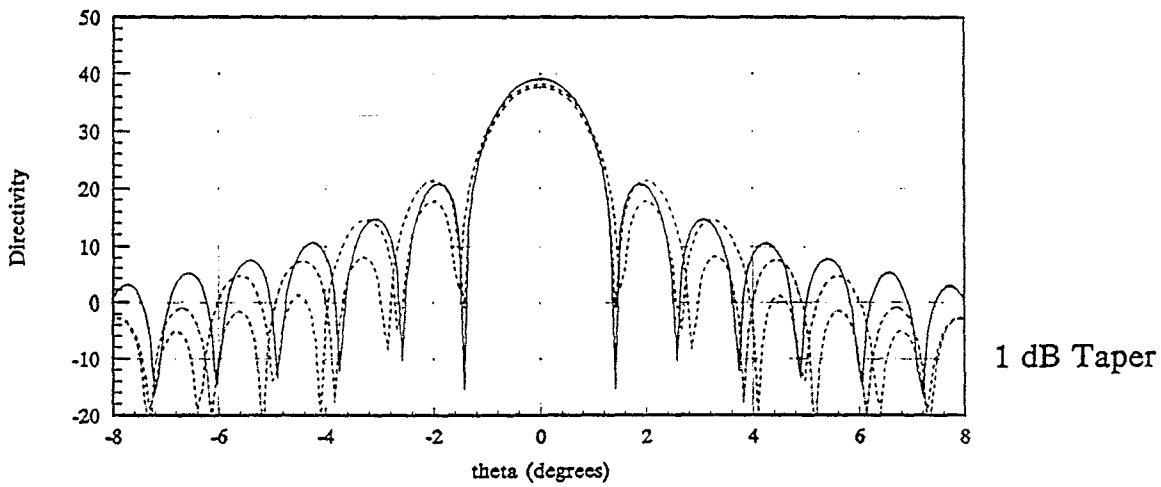
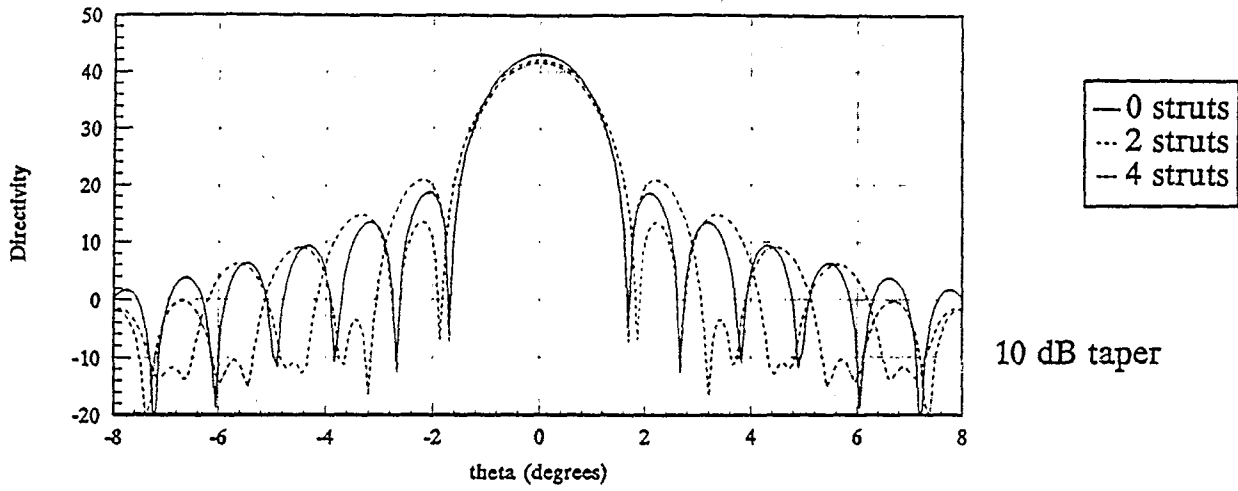


Fig. 1.3. Far field patterns at 3.0 GHz for different combinations of the illumination tapers and blockage (struts) configurations.

f = 1 GHz

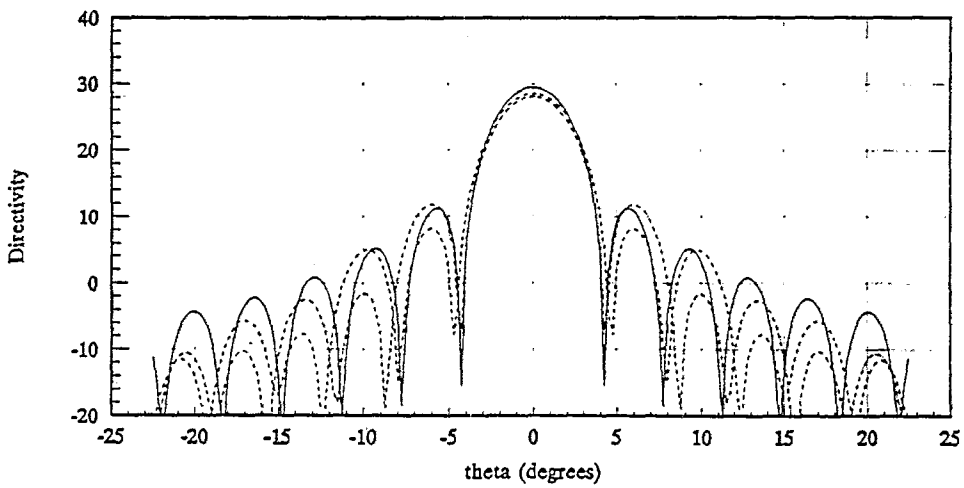
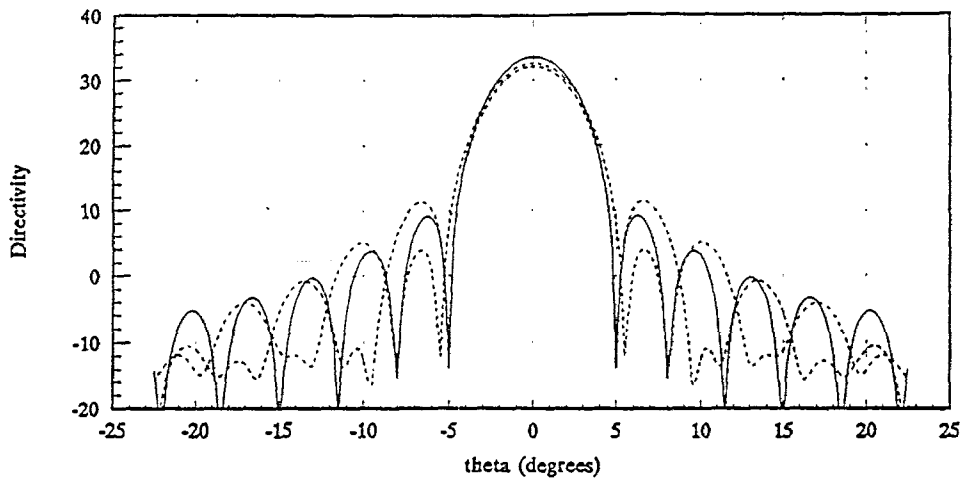


Fig. 1.4. Far field patterns at 1.0 GHz for different combinations of the illumination tapers and blockage (struts) configurations.

f = 0.5 GHz

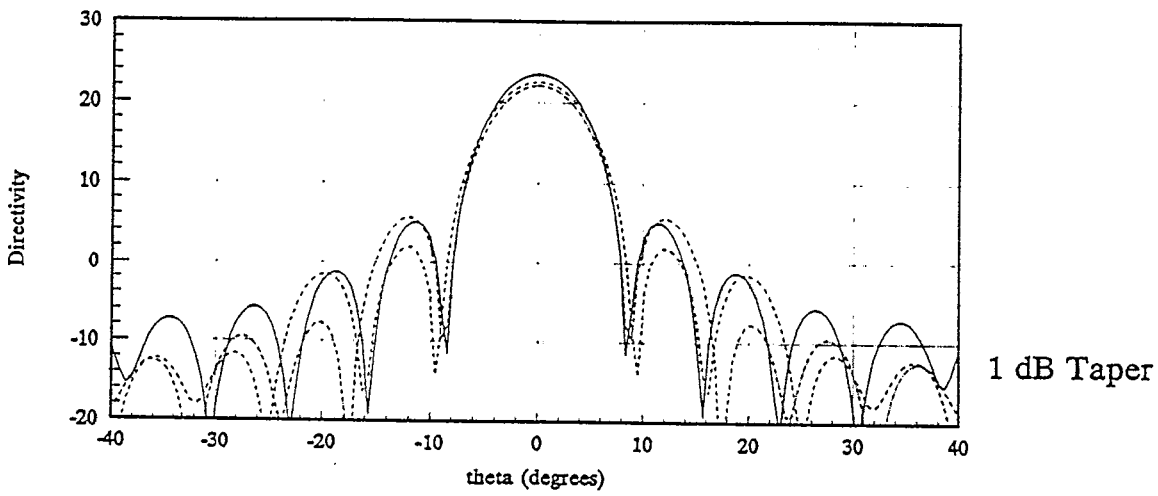
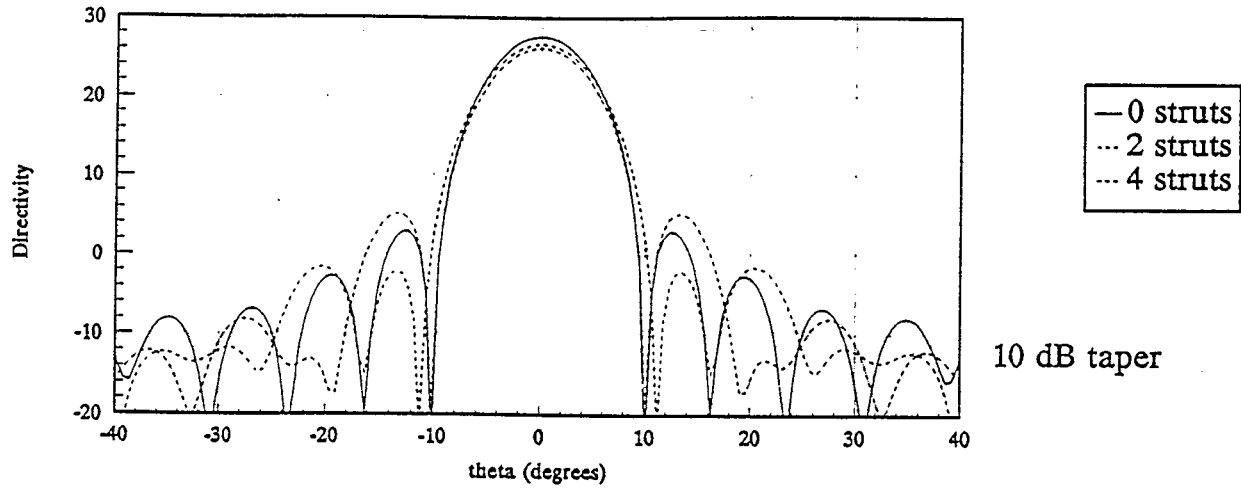


Fig. 1.5. Far field patterns at 0.5 GHz for different combinations of the illumination tapers and blockage (struts) configurations.

f = 0.2 GHz

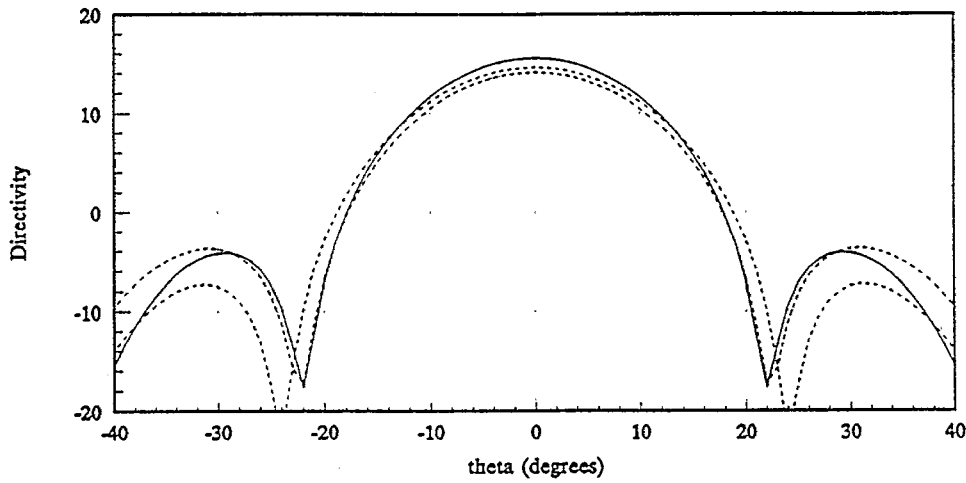
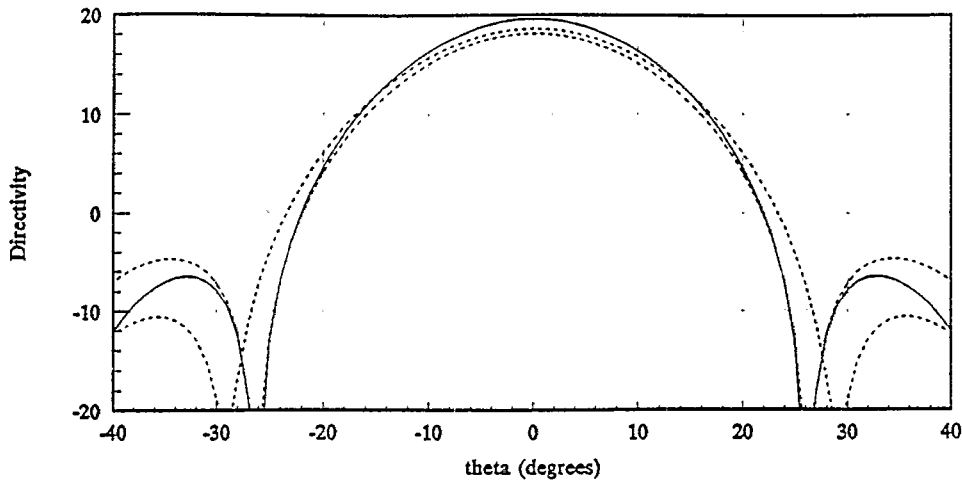


Fig. 1.6. Far field patterns at 0.2 GHz for different combinations of the illumination tapers and blockage (struts) configurations.

## 2. JACOBI-BESSEL SERIES EXPANSION

In this section, we derive some basic identities for the Jacobi-Bessel series expansion as these identities clearly establish our motivation for using the series in the subsequent sections. The Fourier series or trigonometric basis functions can be integrated against the Fourier transform kernel to result in

$$\int_0^{2\pi} \begin{Bmatrix} \cos n\phi' \\ \sin n\phi' \end{Bmatrix} e^{j\xi \cos(\phi' - \phi)} d\phi' = 2\pi j^n \begin{Bmatrix} \cos n\phi \\ \sin n\phi \end{Bmatrix} J_n(\xi), \quad (2.1)$$

where  $J_n$  is the  $n^{\text{th}}$  order Bessel function. Next, we define the modified Jacobi polynomials as

$$F_m^\alpha(s) = \sqrt{2(\alpha + 2m + 1)} P_m^{(\alpha, 0)}(1 - 2s^2) s^\alpha \quad (2.2)$$

where  $\alpha$  is a real number and  $P$  is the Jacobi polynomial obtained from

$$P_m^{\alpha, \beta}(x) = \frac{(-1)^m 2^{-m}}{m!} (1-x)^{-\alpha} (1+x)^{-\beta} \frac{d^m}{dx^m} [(1-x)^{m+\alpha} (1+x)^{m+\beta}] \quad (2.3)$$

which also satisfies the following recurrence relation

$$\begin{aligned} 2(m+1)(\alpha+m+1)(\alpha+2m) P_{m+1}^{(\alpha, 0)}(x) &= [(\alpha+2m)(\alpha+2m+1)(\alpha+2m+2)x \\ &\quad + \alpha^2(\alpha+2m+1)] P_m^{(\alpha, 0)}(x) \\ &\quad - 2m(\alpha+m)(\alpha+2m+2) P_{m-1}^{(\alpha, 0)}(x). \end{aligned} \quad (2.4)$$

The above recurrence relation can be used to generate  $F_m^\alpha$  in (2.2). Furthermore, one can establish the following orthogonality and integration properties for  $F_m^\alpha$ , [3]-[5],

$$\int_0^1 F_m^\alpha(s) F_{m'}^\alpha(s) s ds = \delta_{mm'} = \begin{cases} 1 & m = m' \\ 0 & m \neq m' \end{cases} \quad (2.5)$$

and

$$\int_0^1 F_m^\alpha(s) J_\alpha(\xi s) s ds = \sqrt{2(\alpha + 2m + 1)} \frac{1}{\xi} J_{\alpha+2m+1}(\xi) \quad (2.6)$$

Formulas (2.1), (2.5) and (2.6) are key expressions for the application of the Jacobi-Bessel series to the radiation problems. Figures 2.1-4 are the plots of  $F_m^\alpha$  for various combinations of  $\alpha$  and  $m$ . To generate these plots, a simple computer program has been written based on formulas (2.2) and (2.4).

Having presented some basic identities, we now discuss the Jacobi-Bessel expansion of the integral which appears repeatedly in solving radiation problems. As shown in later sections, the following integral is the central focus of this paper

$$\vec{I}_p(\theta, \phi) = \int_0^1 \int_0^{2\pi} \vec{Q}_p(as', \phi') e^{jkas' \sin\theta \cos(\phi-\phi')} s' ds' d\phi', \quad (2.7)$$

where  $a$  is the radius of the circular region,  $\vec{Q}_p$  is proportional to the field distribution for the aperture antennas and the induced surface current for the reflectors, and  $(\theta, \phi)$  are the observation angles of the spherical coordinates. It is clearly seen that the above integral represents the Fourier transform of the distribution  $\vec{Q}$ . An efficient and accurate evaluation of (2.7) has been a great challenge to researchers dealing with radiation problems. First, note that for each new set of  $(\theta, \phi)$ , integration (2.7) must be re-evaluated repeatedly, which is very time-consuming when the data are needed for many observation points. Second, for large  $a$  or  $\theta$ , the Fourier kernel in (2.7) can oscillate rapidly, again making

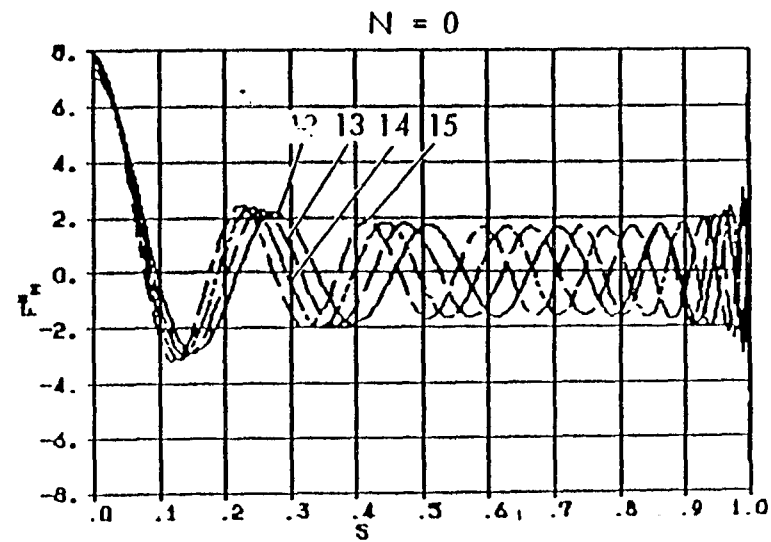
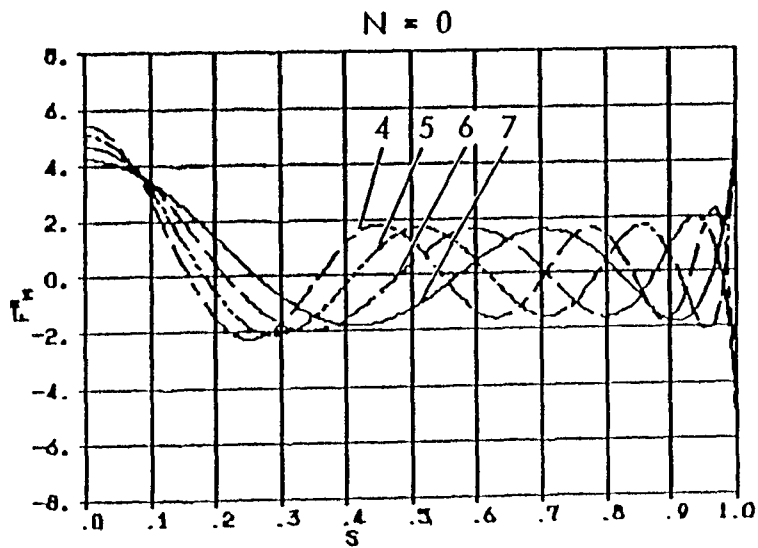
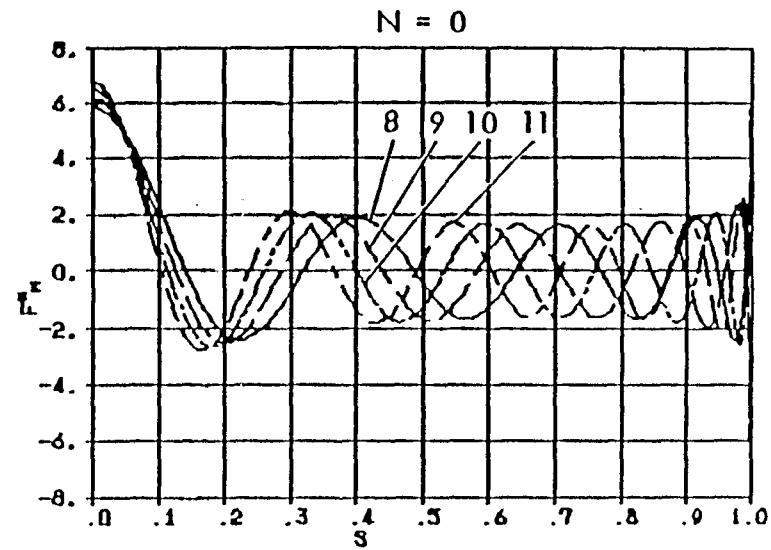
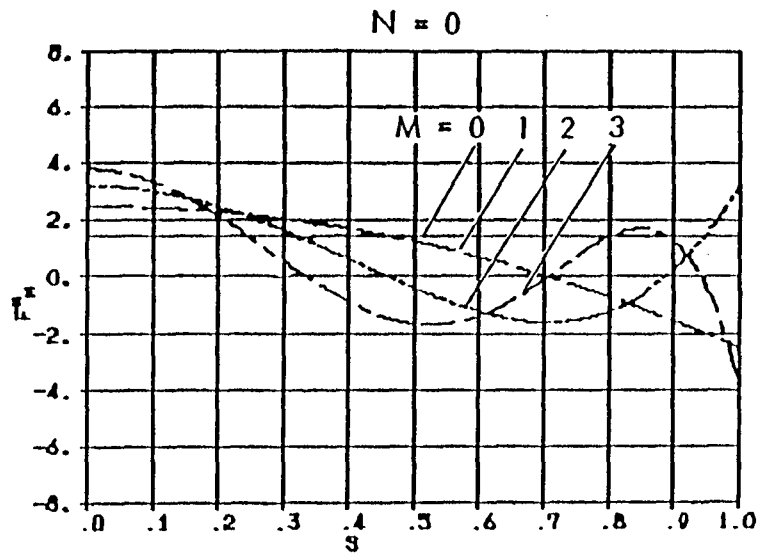


Figure 2.1. Plots of  $F_M^N(s)$  for  $N = 0$  and different values of  $M$ .

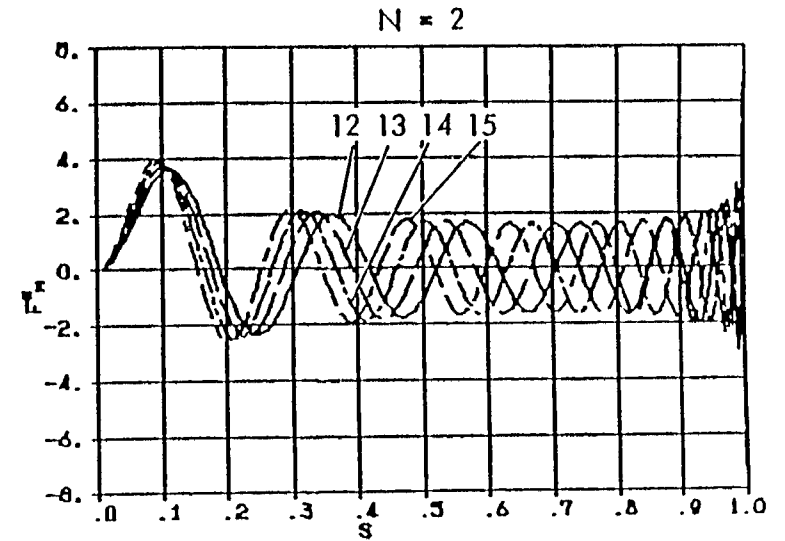
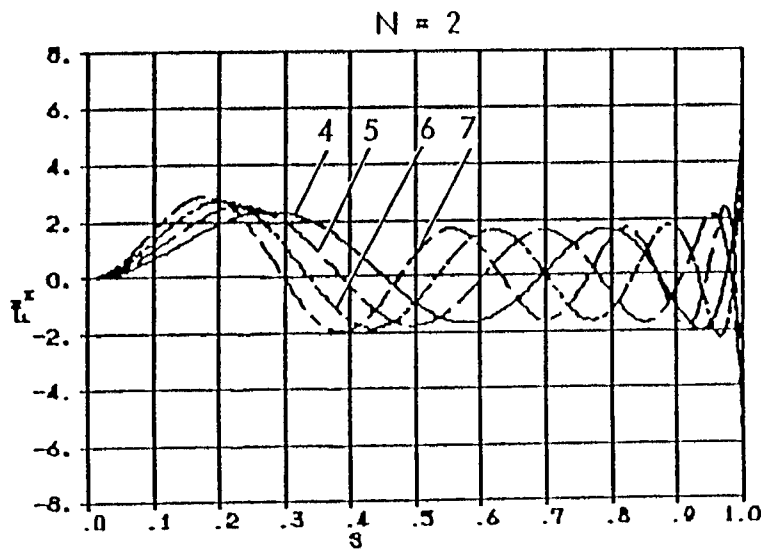
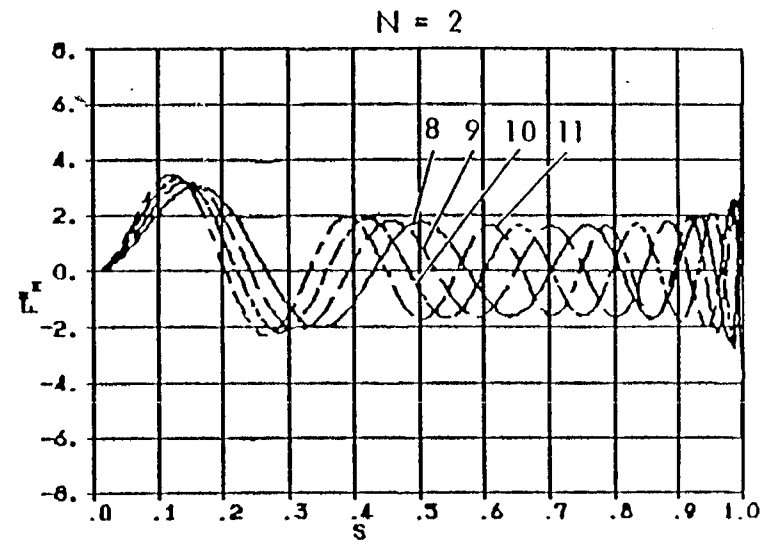
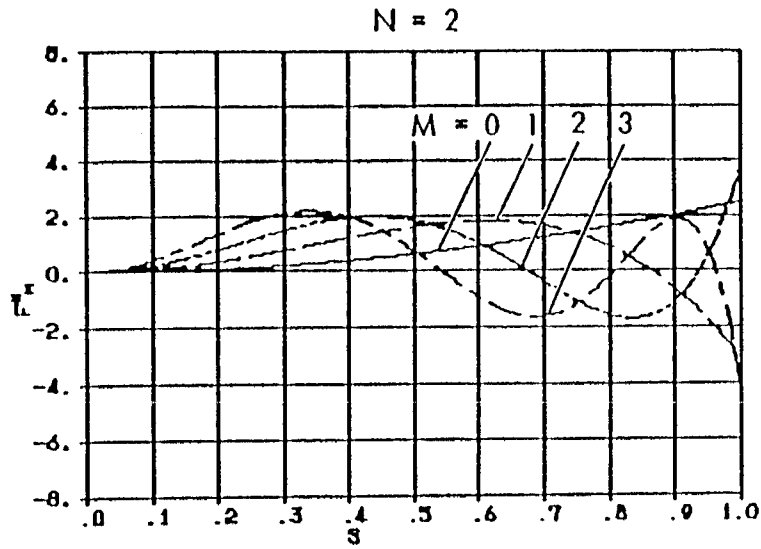


Figure 2.2. Plots of  $F_M^N(S)$  for  $N = 2$  and different values of  $M$ .

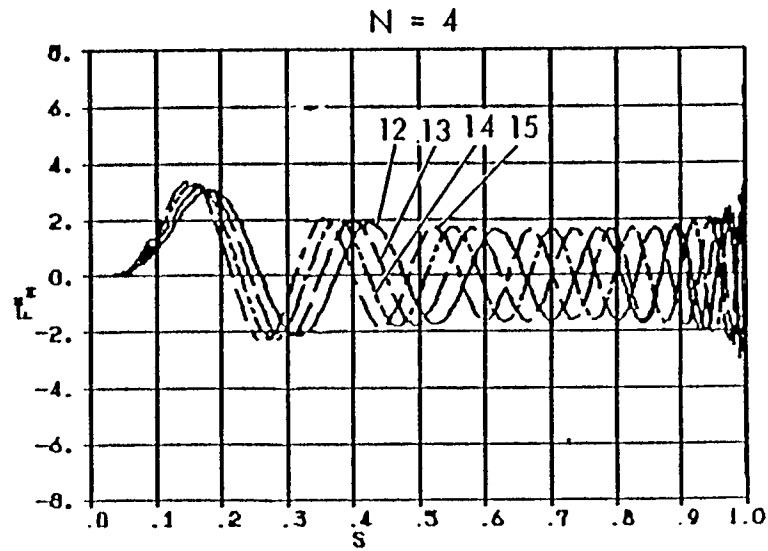
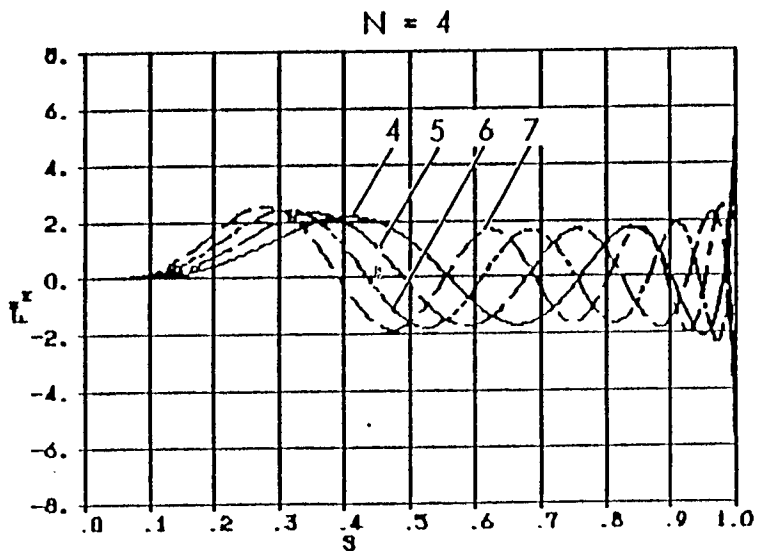
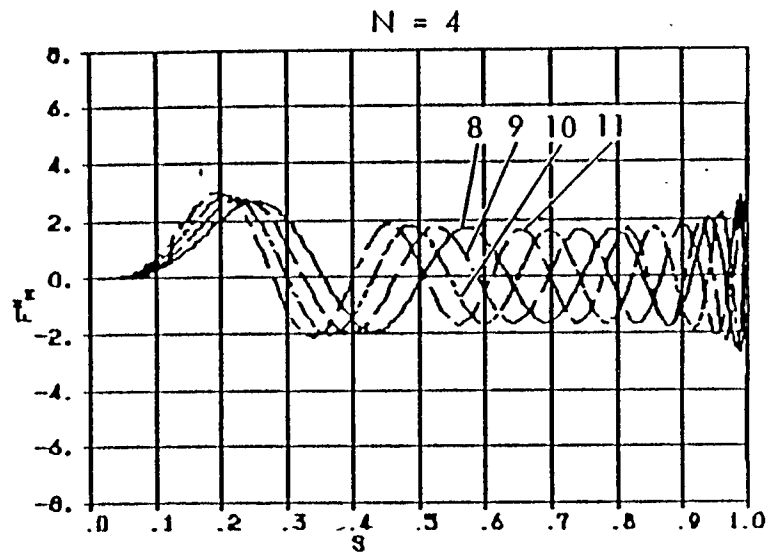
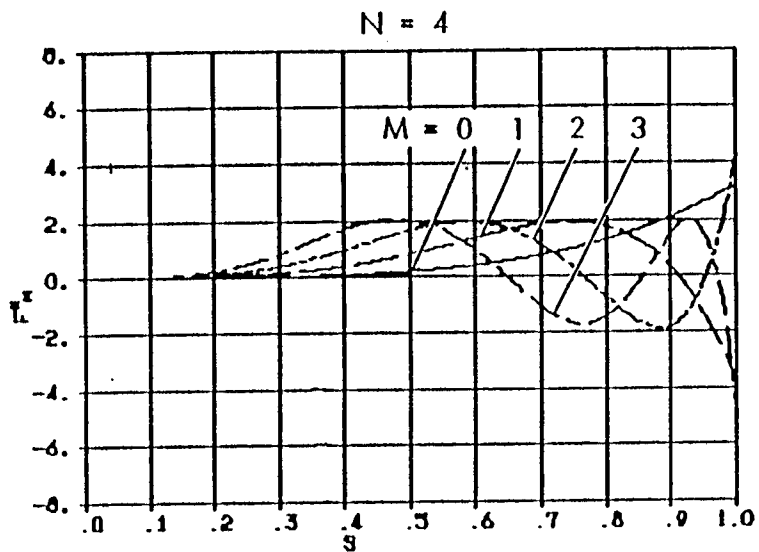


Figure 2.3. Plots of  $F_M^N(S)$  for  $N = 4$  and different values of  $M$ .

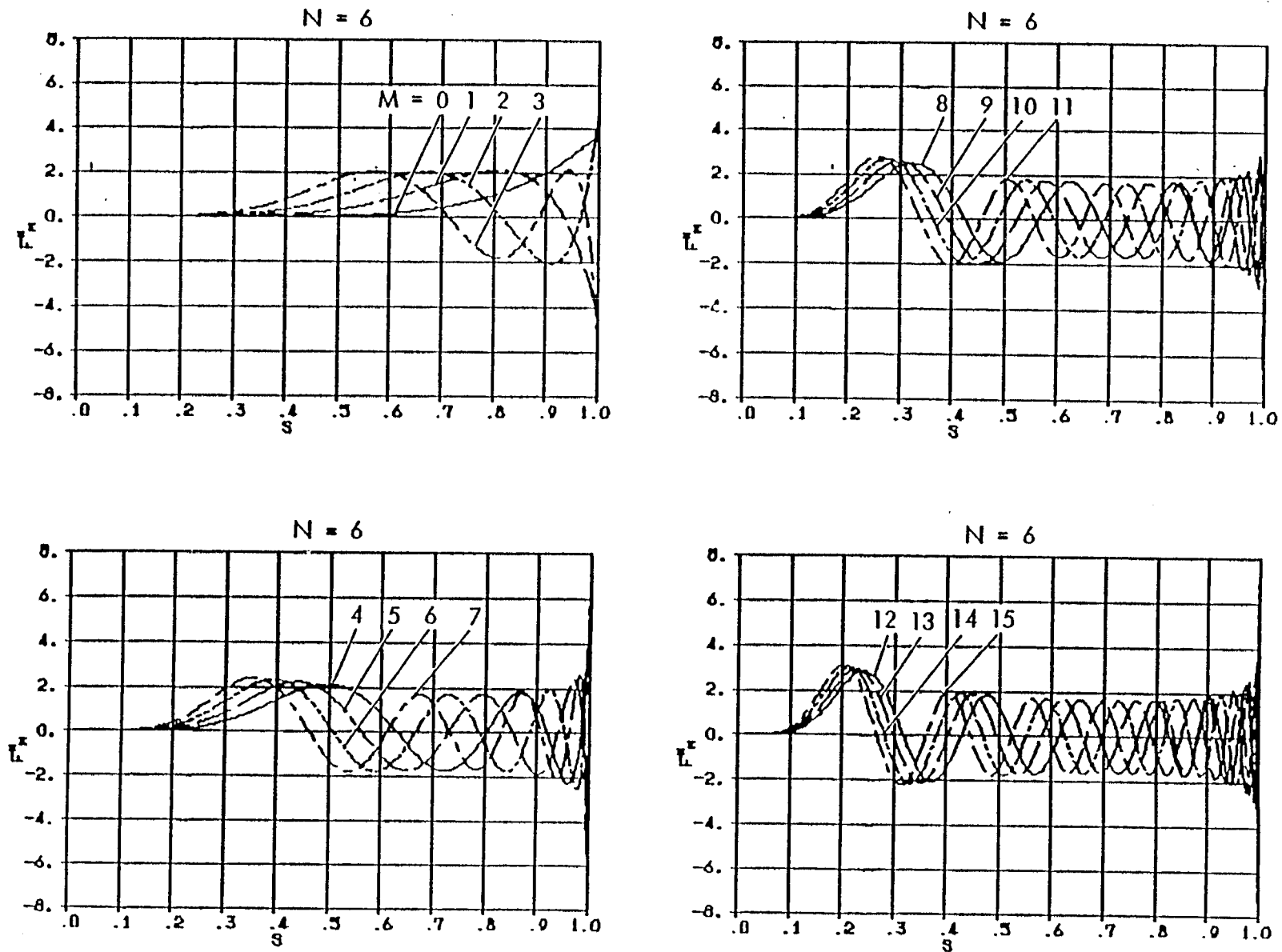


Figure 2.4. Plots of  $F_M^N(s)$  for  $N = 6$  and different values of  $M$ .

the task of numerical evaluation of (2.7) very difficult.

To overcome the above difficulties, we first expand  $\vec{Q}_p(as', \phi')$  using a Fourier series in  $\phi'$  and modified Jacobi polynomials in  $s'$  to arrive at

$$\vec{Q}_p(as', \phi') = \sum_{n=0}^{\infty} \sum_{m=0}^{\infty} [ \vec{C}_{nm} \cos n\phi' + \vec{D}_{nm} \sin n\phi' ] F_m^n(s'), \quad (2.8)$$

where  $\vec{C}_{nm}$  and  $\vec{D}_{nm}$  are constant Cartesian vector coefficients constructed using the orthogonality properties of the expansion functions, i.e., (2.5). It can readily be shown that these constants are obtainable from

$$\begin{pmatrix} \vec{C}_{nm} \\ \vec{D}_{nm} \end{pmatrix} = \frac{\epsilon_n}{2\pi} \int_0^{2\pi} \int_0^1 \vec{Q}_p(as', \phi') \begin{pmatrix} \cos n\phi' \\ \sin n\phi' \end{pmatrix} F_m^n(s') s' d\phi' ds', \quad (2.9)$$

where  $\epsilon_n$  is the Neumann constant obtained in the Fourier series expansion and takes the following values

$$\epsilon_n = \begin{cases} 1 & n = 0 \\ 2 & n \neq 0 \end{cases}. \quad (2.10)$$

Substituting (2.8) into (2.7) and using (2.6), we can finally express  $\vec{I}_p$  as

$$I_p(\theta, \phi) = 2\pi \sum_{n=0}^{\infty} \sum_{m=0}^{\infty} j^n [ \vec{C}_{nm} \cos n\phi + \vec{D}_{nm} \sin n\phi ] \sqrt{2(n+2m+1)} \frac{J_{n+2m+1}(ka \sin\theta)}{ka \sin\theta} \quad (2.11)$$

Some important features of (2.11) may be summarized as follows: (i) once  $\vec{C}_{nm}$  and

$\vec{D}_{mn}$  are determined, they can be used for all observation angles; (ii) the dominant behavior in the vicinity of  $\theta = 0$  is the well-known Airy disc function  $J_1(\xi)/\xi$ ; (iii) the numerical evaluation of (2.9) is much simpler than that of (2.7) as its integrand does not contain the highly oscillatory Fourier transform kernel of (2.7).

The numerical convergence characteristics of (2.11) are discussed in detail in later sections where some practical problems are considered. For each combination of  $p$ ,  $n$  and  $m$ , the integration (2.9) should be evaluated numerically. However, it can be shown that, for many problems of practical interest,  $\vec{Q}_p$  has a quadratic dependence on the variable  $s'$ , namely,

$$\vec{Q}_p(as', \phi') = \vec{K}(as', \phi')(1 - s'^2)^p. \quad (2.12)$$

The above special form permits the application of a very useful upward recursion relationship among the higher-order terms. To this end, it can be shown that

$$\begin{aligned} p B_{nm} = & \sqrt{\frac{n+2m+1}{n+2m-1}} \cdot a_{nm} \cdot (p-1) B_{n(m-1)} \\ & + (b_{nm} - 1) \cdot p^{-1} B_{nm} + \sqrt{\frac{n+2m+1}{n+2m+3}} \cdot c_{nm} \cdot (p-1) B_{n(m+1)}, \end{aligned} \quad (2.13)$$

where  $B$  represents any Cartesian component of either the  $\vec{C}$  or  $\vec{D}$  coefficients, and

$$\left\{ \begin{aligned} a_{nm} &= -\frac{m(n+m)}{(n+2m)(n+2m+1)} \\ b_{nm} &= \frac{(m+n)^2}{(n+2m)(n+2m+1)} + \frac{(m+1)^2}{(n+2m+2)(n+2m+1)} \\ c_{nm} &= -\frac{(m+1)(n+m+1)}{(n+2m+1)(n+2m+2)}. \end{aligned} \right. \quad (2.14)$$

Note that the higher-order  $p$  terms are obtained from the lower-order  $p-1$  terms. We should also note that  ${}_p B_{nm} = 0$  when  $m$  is negative. Therefore, once  ${}_0 \vec{C}_{nm}$  and  ${}_0 \vec{D}_{nm}$  are constructed, all higher-order  $p$  terms can be determined by using a simple algebraic recursion. It is worthwhile to mention that, based on the functional characteristics of the integrand in (2.9), different numerical integration algorithms may be used to evaluate (2.9) and, furthermore, the double summation in (2.11) may be added up for different combinations of  $N$  and  $M$  terms to assure convergence.

### 3. REFLECTOR ANTENNA ANALYSIS

In this section, the Physical Optics (PO) vector radiation integral is first constructed for an offset shaped reflector illuminated by an arbitrarily located and oriented source. A novel procedure is then discussed for expressing the radiation integral in terms of a summation (series) of Fourier transforms of an "effective" aperture distribution which includes the effect of the curvature of the surface. It is shown that this series has a biconvergent nature and can be related to the asymptotic evaluation of the integral. Finally, the Fourier transform integrals are expressed in terms of the Jacobi-Bessel series expansion. Numerical results are presented for different reflector configurations and source locations and comparisons are made with other available data.

#### 3.1 Basic Formulations

Reflector surface  $\Sigma$  is constructed by intersecting a circular cylinder with a doubly curved surface. As depicted in Figure 3.1, the cylinder axis lies along the z-axis and the x-y plane is taken as a plane perpendicular to this axis. We refer to the (x,y,z) system as the reflector unprimed coordinate system and define (x',y',z') as its primed counterpart. The latter is used for defining the integration variables. Construction of the physical optics radiation integral requires knowledge of the incident magnetic field on the reflector surface. For most of the examples considered in this paper, it is assumed that the reflector is in the far-field zone of the source with the phase center of the source located at S with coordinates  $\vec{s} = (s_1, s_2, s_3)$ . Typically, the far field of the source is given in its most convenient coordinate system. We define this system with its Cartesian (x<sub>s</sub>, y<sub>s</sub>, z<sub>s</sub>) coordinates as shown in Figure 3.1. The magnetic far field of the source can be expressed as

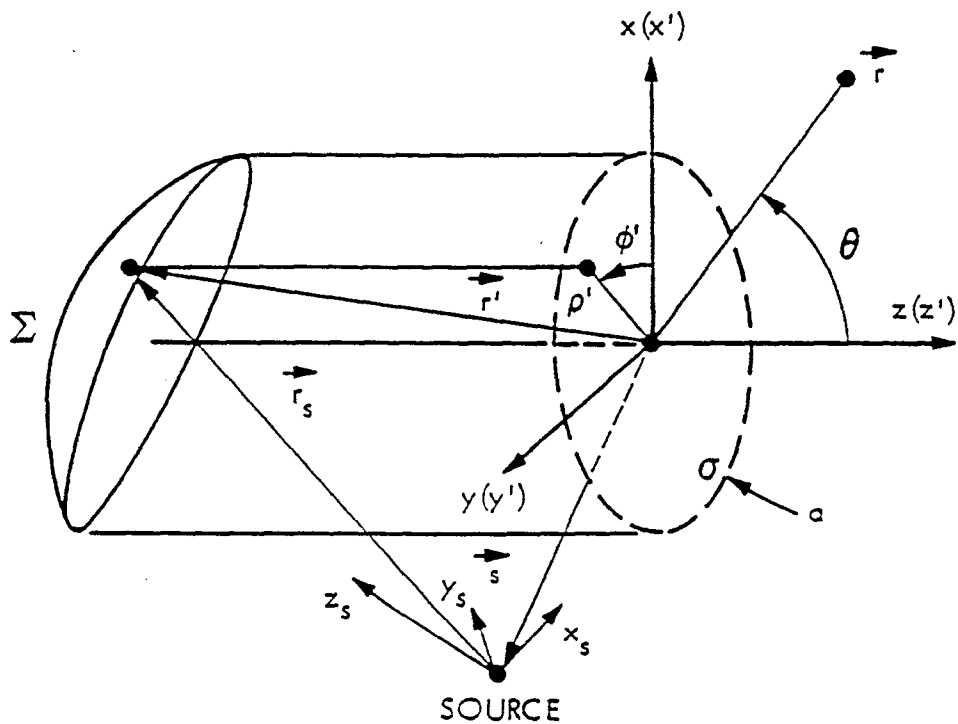


Figure 3.1. Offset reflector antenna illuminated by an arbitrary located source.  $(x, y, z)$  and  $(x_s, y_s, z_s)$  are the reflector and source (feed) coordinates, respectively.

$$\vec{H}_s(\vec{r}_s) = \frac{1}{\eta} \left[ -V(\theta_s, \phi_s) \hat{\theta}_s + U(\theta_s, \phi_s) \hat{\phi}_s \right] \frac{e^{-jk r_s}}{4\pi r_s} \quad (3.1)$$

where  $U$  and  $V$  are the E-pattern functions and  $\eta = \sqrt{\mu/\epsilon}$ . The incident field (3.1) can be expressed in the reflector coordinate system  $(x', y', z')$  using the coordinate transformations based on the Eulerian angles [6] as discussed in Appendix A.

In systems  $(x', y', z')$  and  $(\rho', \phi', z')$ , the surface  $\Sigma$  is described as

$$z' = f(x', y') = \bar{f}(\rho', \phi') \quad \vec{\rho}' \in \sigma \quad (3.2)$$

and its unit normal  $\hat{n}$  is given by

$$\hat{n} = \vec{N}/N \quad (3.3)$$

where

$$\vec{N} = \left[ -\frac{\partial f}{\partial x'} \hat{x} - \frac{\partial f}{\partial y'} \hat{y} + \hat{z} \right] . \quad (3.4)$$

The induced physical optics current on  $\Sigma$  due to the source field is

$$\vec{J} = 2\hat{n} \times \vec{H}_s(\vec{r}') \quad (3.5)$$

where  $\vec{H}_s$  can be constructed from (3.1). Introducing the usual far-field approximation, one can readily arrive at the following far-field expression, viz.,

$$\vec{E} = -jk\eta \frac{e^{-jkr}}{4\pi r} (T_\theta \hat{\theta} + T_\phi \hat{\phi}) + O(r^{-2}) \quad (3.6)$$

where

$$\vec{T}(\theta, \phi) = \int_{\Sigma} \vec{J}(\vec{r}') e^{jk\vec{r}' \cdot \hat{r}} ds' \quad (3.7)$$

Integration (3.7) is performed on the reflector surface  $\Sigma$ . This integration can be transformed into an integration over the projected circular region (dotted circle in Figure 3.1) with the help of the surface Jacobian transformation. By using (3.2), the Jacobian can be expressed as

$$J_{\Sigma} = \sqrt{1 + \left(\frac{\partial f}{\partial \rho'}\right)^2 + (\rho')^{-2} \left(\frac{\partial f}{\partial \phi'}\right)^2} \quad (3.8)$$

which allows one to express the radiation integral (3.7) as

$$\vec{T}(\theta, \phi) = \int_0^a \int_0^{2\pi} \vec{J}(\rho', \phi') [e^{jkr' \cos\theta' \cos\theta}] \cdot \{e^{jk\rho' \sin\theta \cos(\phi' - \phi)}\} \rho' d\rho' d\phi' \quad (3.9)$$

where

$$\vec{J}(\rho', \phi') = \vec{J}(\vec{r}') J_{\Sigma} = 2\vec{N} \times \vec{H}_s(\vec{r}') \quad (3.10)$$

It is readily observed that  $\vec{J}$  depends only on the primed coordinates, whereas the remainder of the integrand depends on both the primed and unprimed coordinates. The factor  $\{\exp[jk\rho' \sin\theta \cos(\phi' - \phi)]\}$  is the polar form of the Fourier transform kernel. The remaining factor  $\{\exp[jkr' \cos\theta' \cos\theta]\} = \{\exp[jkz' \cos\theta]\}$  must remain under the integral as long as the reflector has curvature, i.e.,  $z'$  not equal to a constant or linear term. Radiation integral (3.9) can be numerically evaluated in a direct manner for every observation point. Unfortunately, this scheme is very time-consuming even on modern computers for large reflectors and many observation points. Our task in the following sections is to recast (3.9) in a form suitable for an efficient and accurate numerical evaluation.

### 3.2 Rearranging the Radiation Integral

We now proceed to rearrange the integrand of (3.9) in a manner which will allow us to integrate on the curved reflector surface with only slightly more effort than would be necessary for integration on a flat surface. The procedure follows similar steps as in [1], [2]. As the starting point, we assume that the scattered field has its pencil beam directed toward  $(\theta_B, \phi_B)$  and try to rearrange the Fourier kernel  $\{\cdot\}$  such that its center is in this direction. To this end, we write (3.9) as

$$\vec{T}(\theta, \phi) = \int_0^a \int_0^{2\pi} \vec{K}(\rho', \phi') [e^{jk\rho' \cos\theta' \cos\theta}] \cdot e^{jk\rho' B \cos(\phi' - \phi)} \rho' d\rho' d\phi' \quad (3.11)$$

where

$$\vec{K}(\rho', \phi') = \vec{J}(\rho', \phi') e^{-jk\rho'(C_u \cos\phi' + C_v \sin\phi')} \quad (3.12)$$

and

$$C_u = -\sin\theta_B \cos\phi_B \quad (3.13a)$$

$$C_v = -\sin\theta_B \sin\phi_B \quad (3.13b)$$

$$B = \sqrt{(\sin\theta \sin\phi + C_v)^2 + (\sin\theta \cos\phi + C_u)^2} \quad (3.14a)$$

$$\phi = \tan^{-1} \frac{\sin\theta \sin\phi + C_v}{\sin\theta \cos\phi + C_u} \quad (3.14b)$$

It is crucial to note that, when  $\theta = \theta_B$  and  $\phi = \phi_B$ , we find  $B = 0$ .

We now focus our attention on the  $[\cdot]$  term, which is a function of both the observation and the source coordinates. We define the following functional notation:

$$L = L(\rho', \phi'; \theta) = r' \cos \theta' \cos \theta = z' \cos \theta = \tilde{f}(\rho', \phi') \cos \theta \quad (3.15)$$

with the help of (3.2). Similarly, we introduce more functionals obtained from (3.15), namely,

$$L_0 = L(\rho', \phi'; \theta_0) = \tilde{f}(\rho', \phi') \cos \theta_0 = z' \cos \theta_0 \quad (3.16a)$$

$$L_w = L(\rho_w', \phi_w'; \theta) = \tilde{f}(\rho_w', \phi_w') \cos \theta = z_w' \cos \theta \quad (3.16b)$$

$$L_{w0} = L(\rho_w', \phi_w'; \theta_0) = \tilde{f}(\rho_w', \phi_w') \cos \theta_0 = z_w' \cos \theta_0 \quad (3.16c)$$

where  $z_w'$  and  $\theta_0$  are fixed values of  $z_w'$  and  $\theta_0$  (to be chosen later). In (3.16),  $\theta_0$  is a fixed angle typically taken along the beam maximum and usually set to be  $\theta_0 = \theta_B$  ( $\theta_B$  was defined in the previous section).  $(\rho_w', \phi_w')$  are the coordinates of a specular point on the reflector which provides the dominant contributions to a given wide angle observation point. Typically, this point is located on the rim where  $\rho_w' = a$  (for angles far from the beam maximum [typically  $> 3$  sidelobes], the specular points are on the rim). Employing (3.15) and (3.16), we define  $\Delta$  as follows

$$\Delta = L - L_0 - L_w + L_{w0} = [\tilde{f}(\rho', \phi') - \tilde{f}(\rho_w', \phi_w')](\cos \theta - \cos \theta_0) \quad (3.17)$$

which has the following property

$$\Delta \rightarrow 0 \text{ as } \theta \rightarrow \theta_0 \text{ and/or as } (\rho', \phi') \rightarrow (\rho_w', \phi_w') \quad (3.18)$$

Introducing  $\Delta$  into (3.7) and using the Taylor series expansion

$$e^{jk\Delta} = \sum_{p=0}^{P \rightarrow \infty} \frac{1}{p!} (jk\Delta)^p \quad (3.19)$$

we finally arrive at [2]

$$\tilde{T}(\theta, \phi) = \sum_{p=0}^{P \rightarrow \infty} \tilde{T}_p(\theta, \phi) \quad (3.20)$$

where

$$\begin{aligned} \tilde{T}_p(\theta, \phi) = & \frac{1}{p!} (jk)^p e^{jk(L_w - L_{w0})} (\cos\theta - \cos\theta_0)^p \\ & \cdot \int_0^{2\pi} \int_0^a \frac{1}{K} e^{jkL_0} [\bar{f}(\rho', \phi') - \bar{f}(\rho'_w, \phi'_w)]^p \\ & \cdot e^{jk\rho' B \cos(\phi' - \phi)} \rho' d\rho' d\phi' \quad (3.21) \end{aligned}$$

In its present form, expansion (3.20) is rapidly convergent at observation angles near  $\theta_0$  and those near the observation points with their specular points located at  $(\rho'_w, \phi'_w)$ . Thus, this expansion is convergent near two different observation values and is thus termed "biconvergent." Clearly, it will be very useful to be able to extend the rapid convergence domain of (3.20). Notice that, at wide observation angles the dominant contribution to integration (3.21) is from the point near  $(\rho'_w, \phi'_w)$  where the integrand is negligible as  $p$  increases. In later discussions, we demonstrate how the rapid convergence domain of (3.20) can be expanded.

Having obtained (3.21), our task is now to evaluate the integration appearing in it. For simplicity of notation, we use (3.21) to define  $I_p$

$$\vec{I}_p(\theta, \phi) = \int_0^{2\pi} \int_0^1 \vec{Q}_p(as', \phi') e^{jkas' B \cos(\phi' - \phi)} s' ds' d\phi' \quad (3.22)$$

where

$$\vec{Q}_p(as', \phi') = \vec{K}(as', \phi') e^{jkL_0} [\bar{f}(\rho', \phi') - \bar{f}(\rho'_w, \phi'_w)]^p \quad (3.23)$$

It is readily apparent that (3.22) has a form identical to (2.7), which, therefore, allows one to expand it in terms of the Jacobi-Bessel series as in (2.11). Omitting all the intermediate steps, we can finally construct the following expression [2]

$$\begin{aligned} \vec{T}(\theta, \phi) &= 2\pi a^2 e^{jk(L_w - L_{w0})} \sum_{p=0}^{P \rightarrow \infty} \frac{1}{p!} (jk)^p (\cos\theta - \cos\theta_0)^p \\ &\cdot \sum_{n=0}^{N \rightarrow \infty} \sum_{m=0}^{M \rightarrow \infty} j^n [{}_p \vec{C}_{nm} \cos n\phi + {}_p \vec{D}_{nm} \sin n\phi] \\ &\cdot \sqrt{2(n+2m+1)} \frac{J_{n+2m+1}(kaB)}{kaB} \quad (3.24) \end{aligned}$$

The above result can be used in (3.6) for the determination of the far-field pattern.

For offset reflectors, expression (3.2) is, in general, a function of  $\phi'$  which, in turn, makes (3.16) the edge spectral point for wide angle radiation, dependent on  $\phi'$ . In contrast to the symmetric case where the domain of (3.18) is extended to all points on the rim by simply setting  $\rho'_w = a$ , this domain cannot be extended so simply for the offset reflectors. It is, in addition, worthwhile to emphasize that, as far as the numerical evaluation of (3.24) is concerned, it is



still desirable to obtain a biconvergent series for as many wide angles of observation points as possible. To achieve this goal, we consider what occurs for offset parabolic reflectors. As shown in [2], it is still possible to obtain a biconvergent p series for all  $\phi'_w$ .

The offset parabolic surface description for Figure 3.2 can be written as

$$z' = F \left[ -1 + \frac{\rho'^2}{4F^2} \right] + \frac{h}{2F} \rho' \cos \phi' + \frac{h^2}{4F} \quad (3.25)$$

where F and h designate the focal length and offset height, respectively. A unique feature of (3.25) is the appearance of the linear term in  $\rho'$  and  $\cos \phi'$ . Since this is the only term dependent on  $\phi'$ , it is desirable to transplant it into the Fourier kernel. To do this, we combine this term with the Fourier kernel term of (3.11) and express (3.13) and (3.14) by

$$\begin{cases} C_u = -\sin \theta_B \cos \phi_B - \frac{h}{2F} \cos \theta_B \\ C_v = -\sin \theta_B \sin \phi_B \end{cases} \quad (3.26)$$

and

$$\begin{cases} B = \sqrt{(\sin \theta \sin \phi + C_v)^2 + (\sin \theta \cos \phi + C_u + \frac{h}{2F} \cos \theta)^2} \\ \phi = \tan^{-1} \frac{\sin \theta \sin \phi + C_v}{\sin \theta \cos \phi + C_u + (h/2F) \cos \theta} \end{cases} \quad (3.27)$$

Furthermore, we redefine a new functional L from (3.15) as

$$L = F \left[ -1 + \frac{\rho'^2}{4F^2} \right] \cos \theta \quad (3.28)$$

which finally results in

$$\Delta = \frac{1}{4F} (\rho^{-2} - a^2) (\cos\theta - \cos\theta_0) \quad (3.29)$$

which has a form similar to (3.17). Following the same steps as in (3.19)-(3.24), we can finally construct  $\bar{I}_p$  and  $\bar{T}(\theta, \phi)$ . Because of the special  $\rho^{-2}$  dependence in (3.29), one can employ a recursion relation to derive the higher-order terms of the  $p$  series from its  $p = 0$  term. The details of this procedure have already been given in Section 2 in accordance with (2.12)-(2.14). The fact that the recursion relation can be used in this case is a very unique characteristic of the symmetric and offset parabolic reflectors.

## REFERENCES

- [1] Rahmat-Samii, Y., R. Mittra, and V. Galindo-Israel, "Computation of Fresnel and Fraunhofer Fields of Planar Apertures and Reflector Antennas by Jacobi-Bessel Series - A Review," Electromagnetics, Hemisphere Publishing Corp., Volume 1, Number 2, April-June 1981, pp. 155-185.
- [2] Rahmat-Samii, Y. and V. Galindo-Israel, "Shaped Reflector Antenna Analysis Using the Jacobi-Bessel Series," IEEE Transactions on Antennas and Propagation, Volume AP-28, Number 4, July 1980, pp. 425-435.
- [3] Magnus, W., F. Oberhettinger and R. P. Soni, Formulas and Theorems for the Special Functions of Mathematical Physics, New York: Springer-Verlag, 1966.
- [4] Bateman Manuscript Project, Tables of Integral Transforms, Vol. II, New York: McGraw-Hill, 1954.
- [5] Slepian, D., "Prolate Spheroidal Wave Functions, Fourier Analysis and Uncertainty-IV: Extensions to Many Dimensions; Generalized Prolate Spheroidal Functions," Bell Syst. Tech. J., Vol. 43, pp. 3009-3057, July-December 1964.
- [6] Rahmat-Samii, Y., "Useful Coordinate Transformations for Antenna Applications," IEEE Transactions on Antennas and Propagation, Volume AP-27, July 1979, pp. 571-574.
- [7] Rahmat-Samii, Y. and S. W. Lee, "Directivity of Planar Array Feeds for Satellite Reflector Applications," IEEE Transactions on Antennas and Propagation, Volume AP-31, May 1983, pp. 463-470.
- [8] Ludwig, A. C., "The Definition of Cross Polarization," IEEE Transactions Antennas and Propagation, Volume AP-21, Number 1, January 1973, pp. 116-119.
- [9] Baum, C. E., "Radiation of Impulse-Like Transient Fields, Sensor and Simulation Note 321, November 1989.
- [10] Baum, C. E., "Configurations of TEM Feed for an IRA ", Sensor and Simulation Note 327, 27 April 1991.
- [11] Farr, E. G., "Analysis of the Impulse Radiating Antenna ", Sensor and Simulation Note 329, 24 July 1991.
- [12] Farr, E. G., "Simple Models of Antennas Useful in Ultra-Wideband Applications ", Transient Radiating Antenna Memos, Memo 2, July 1992.
- [13] Farr, E.G., "Prepulse Associated with the TEM Feed of an Impulse Radiating Antenna ", Sensor and Simulation Note 337, March 1992.